



Wing Load and Angle-of-Attack Identification Using Optical Fiber Sensors and Neural Networks

| | |
|--|--|
| Journal: | <i>AIAA Journal</i> |
| Manuscript ID | 2018-07-J057767.R1 |
| Manuscript Type: | Regular Article |
| Date Submitted by the Author: | n/a |
| Complete List of Authors: | Wada, Daichi; Japan Aerospace Exploration Agency, Aeronautical Technology Directorate Tamayama, Masato; Japan Aerospace Exploration Agency, Aeronautical Technology Directorate |
| Subject Index Category: | 00100 Aerodynamics < 00000 AIRCRAFT TECHNOLOGY, CONVENTIONAL, STOL/VTOL |
| Select ONE Subject Index for the Table of Contents. This is where your paper will show up in the Table of Contents: | 00000 AIRCRAFT TECHNOLOGY, CONVENTIONAL, STOL/VTOL |
| | |

SCHOLARONE™
Manuscripts

Wing Load and Angle-of-Attack Identification Using Optical Fiber Sensors and Neural Networks

Daichi Wada,¹ and Masato Tamayama²
Japan Aerospace Exploration Agency, Mitaka-shi Osawa, Tokyo, 181-0015, Japan

The load and angle of attack (AoA) are critical parameters to be monitored for efficient operation of aircraft. This study presents wing load and AoA identification techniques using optical fiber sensors and a neural network approach. We developed a 3.6-m semi-spanned wing model with eight flaps, and bonded two optical fibers with 30 fiber Bragg gratings (FBGs) each along the main and aft spars. Using this model in a wind tunnel test, we demonstrate load and AoA identification through a neural network approach. We input the FBG data and the eight flap angles to a neural network, and output estimated load distributions on the eight wing segments. Thereafter, we identify the AoA by using the estimated load distributions and the flap angles through another neural network. This process requires only the FBG and flap angle data to be measured. We successfully identified the load distributions with an error range of -1.5–1.4 N and a standard deviation of 0.57 N. The AoA was also successfully identified with error ranges of -1.03–0.46° and a standard deviation of 0.38°. We also discussed the identification performances when the variations of wind speeds existed.

I. Introduction

LOAD monitoring techniques for wing structures are a promising technology for enhancing flight performance of future aircraft. Load monitoring is beneficial in terms of structural safety and reliability. There has been significant demand for high-aspect-ratio wings for efficient long-endurance flight, and the loading to such structurally challenging designs is critical [1]. Monitoring results of loading history can be utilized for structural fatigue analysis. By controlling applied loads to wings based on real-time load monitoring, it could be feasible to alleviate undesirable large moments at the wing root. When wings are flexible, aerodynamic loads cause large deflections, which affect the

¹ Researcher, Aeronautical Technology Directorate; wada.daichi@jaxa.jp.

² Associate Senior Researcher, Aeronautical Technology Directorate; tamayama.masato@jaxa.jp.

1
2
3 aeroelastic stability and response [2-4]. Load monitoring is beneficial to estimate structural deformation and to conduct
4 reliable structural analysis based on practical assumptions of deflected wing shape. Another potential benefit of load
5 monitoring is stable and efficient control of aircraft, including unmanned air vehicles (UAVs). Considering the gust
6 perturbation process for example, the load variations from oncoming gusts result in attitude and flight path variations,
7 and there is a theoretical phase-lag between the cause (load) and effect (attitude and flight path) [5-7]. The load is a
8 “phase-advanced” phenomena in this sense, and, therefore, its observation in addition to the conventional inertia
9 observations could potentially enhance vehicle controllability.
10
11
12
13
14
15

16 Aerodynamic loads are not always directly measurable. The wing structure is complex and space in wings is
17 limited. It is difficult to install sufficient pressure sensors and tubes. To overcome these engineering obstacles, studies
18 have been conducted to estimate, as opposed to directly measure, the loads using a measurable parameter, which is
19 strain. In a mechanical sense, load causes strain. When strain is used to identify loads, it creates an inverse problem
20 [8-10]. Inverse analyses tend to be ill-conditioned, specifically when distributed aerodynamic loads are to be solved.
21 The solution becomes highly unstable for the measured strain errors. There have been a number of studies to obtain
22 stable solutions. For example, using the inverse interpolation method, Shkarayev et al. assumed polynomial functions,
23 whereas Coates et al. used Fourier cosine series terms for spatial load distribution functions [11,12]. Nakamura et al.
24 reported a finite-element-based inverse analysis in which aerodynamic restriction was coupled with elastic equations
25 [13]. These techniques to assume functions for aerodynamic load distributions are effective in improving the
26 identification accuracy, however, they limit the applicability of the load identification when the target load
27 distributions were not represented by a simple function form. There have been other studies to identify loads, not by
28 inverse analysis, but by using neural networks. Using strain as an input and load as an output of the neural network,
29 the strain-to-load transfer is represented by the neural network that is optimized through a learning algorithm. This
30 approach solves the problem in a direct manner, therefore, stable solutions are expected. Cao et al. conducted
31 numerical simulations of a cantilever beam to validate the neural network applicability [14]. Trivailo et al. used strain
32 gauge data to estimate loads in fatigue tests that simulated maneuver and buffet loads [15]. They reported successful
33 results, although they focused primarily on the load identification in the form of a limited number of concentrated
34 forces. Wada et al. reported that the approach was applicable for the identification of distributed loads by using a
35 number of strain gauges bonded on a flat panel [16]. These techniques remain limited to a level of conceptual
36 demonstration, and validation of the applicability in the aerodynamic environment needs to be conducted. Currently,
37
38
39
40
41
42
43
44
45
46
47
48
49
50
51
52
53
54
55
56
57
58
59
60

one of the primary challenges is the collection of sufficient amounts of strain data from the wing structure under flight conditions.

It is not practical to install a myriad strain gauges on the surface of the wings considering the amount of wiring required. Digital image correlation technique would be a candidate to efficiently observe strain distribution profiles and there is a successful example to measure strains for load estimation of membrane wings in wind tunnel tests [17], however, some difficulties arise for in-flight uses. Stable setup of observation devices is not always available specifically when small UAVs are assumed and the observed images are under strong influence of flight environments such as the weather. On the other hand, recent studies indicate that optical fiber sensors are potentially promising techniques for obtaining strain information. By measuring multiple strains in a distributed manner along a single fiber, optical fiber sensing exhibits significant effectiveness for collecting great volumes of data for wing and blade structures [18, 19]. The sensing fibers are lightweight, thin, and can be attached to the surface of wings with only marginal effect on the flight performance. A number of studies have demonstrated the feasibility of monitoring wings in wind tunnel tests [20] and UAV wings in flight using fiber Bragg gratings (FBGs) [21-23]. Multiple FBGs inscribed along fibers successfully measured strain distributions, and enabled discussions about usage conditions, such as wing deformation.

In this study, we utilize an optical fiber sensing technique to measure strain distributions on the wing surface and demonstrate load identification by the neural network approach in a wind tunnel test. A 3.6-m semi-spanned high-aspect-ratio wing model, with eight flaps on the trailing edge that enables arbitrary variations of load distributions, was developed. Two optical fibers with 30 FBGs each were bonded along the main and aft spars, and measured strain distributions in a wavelength-division-multiplexing manner [24]. Aerodynamic loads were applied in a wind tunnel, and load distributions were identified by using the FBG and data from the eight flap angles through a neural network. The focus of this study is not limited to aerodynamic loads. Considering the wider applicability of neural networks for aerodynamic parameter identification, we examine other parameter identification, the angle of attack (AoA). The AoA is also one of the essential parameters that has a significant effect on static and dynamic response of high-aspect-ratio wings [2-4]. We propose an identification process for loads and AoAs that requires only the FBG and flap angle data to be measured. We illustrate the applicability of the neural network through experimental results and discussions, and demonstrate the effect of the integration of the optical fiber sensing and the neural network techniques for wing structures.

II. Materials and Methods

A. Wing Model with Multiple Flaps and Optical Fiber Sensors

We developed a 3.6-m semi-spanned wing model with eight flaps on the trailing edge. The wing structure had balsa wood main and aft spars and skin. Woven carbon fiber reinforced plastic fabrics covered the balsa wood. A 400-mm stainless-steel shaft was inserted from the wing root in the main spar in order to attach the wing model to the wind tunnel base. Figure 1 shows a photograph and a schematic of the wing model. We set Z axis along the span. We labeled the flaps Flap 1, 2, ..., 8 from the wing root. For each wing segment with Flap 1, 2, ..., 8, we listed in Table 1 the position Z of the center of the flap, the span-wise length of the flaps, the chord length of the wing measured at the center of the flaps and the flap width measured in chord-wise. Servomotors (BLS177SV, Futaba) controlled the flap angles. The movable range of the flap angles was from -15° to 15° . The positive angle indicates flap down so that the lift force increases, with zero degrees the neutral setting. We set eight static pressure-port arrays at the center of each wing segment. For each pressure sensor array, there were 15 pressure ports on the upper side and 8 on the lower side. A total 184 silicon tubes for pressure sensors were installed and connected to an interrogator (Electronic Pressure Scanners, Pressure System) that was placed out of the wind tunnel. Figure 2 shows the cross-section of the wing model with the locations of the pressure ports and spars. We set X and Y axes. We labeled the pressure ports on the upper side as u_1, u_2, \dots, u_{15} and on the lower side as l_1, l_2, \dots, l_8 , counting from the leading edge. The normal direction at each pressure port was expressed by θ . Table 2 listed the geometry of the pressure ports at the wing segment of Flap 1. The geometry was not identical but similar for other wing segments. The distributions of the pressure coefficient, C_p , of the wing segment with Flap 1 are shown in Fig. 3. The flap position was neutral. We calculated the applied lift loads on each wing segment by integrating the measured static pressures around the airfoil. By dividing the airfoil into segments as labeled $U_1, U_2, \dots, U_{15}, L_1, L_2, \dots, L_8$ corresponding to each pressure port as seen in Fig. 2, we multiplied the measured pressures with corresponding areas of the segments based on the approximation that the pressures were uniform in the segments. By considering the normal direction, we calculated the lift loads that was the out-of-plane forces on the wing. Figure 4 shows the lift coefficient, C_L , of the wing model with respect to AoA. The positions of the flaps were neutral.

We bonded two optical fibers with inscribed FBGs on the upper side of the wing along the main and aft spars. We inscribed 30 FBGs at 120 mm intervals in individual fibers in order to cover the whole semi-span of the wing. The gauge length of the FBGs was 5 mm and the reflectivity was 70%. We designed the Bragg wavelengths of the 30

FBGs ranging from 1530–1595 nm (in the C- and L-bands) so that we could monitor the individual Bragg spectra in the wavelength-division-multiplexing manner. Figure 5 shows the reflected Bragg spectra from the optical fibers bonded to the main and aft spars. We used FBG interrogation monitors (I-MON 512 USB, Ibsen) to observe the reflected spectra, and could observe 30 FBGs in wavelength domain. The Bragg wavelength intervals were set wider at shorter wavelengths. We aligned the FBGs with shorter Bragg wavelengths closer to the wing root as the wing root was expected to have greater strain variation amplitudes in general, and it was aimed at avoiding spectral overlap.

A wind shield was placed at the wing root. The lead wires of the servomotors, the pressure sensor tubes, and the optical fibers were routed to the basement of the wind tunnel and connected to the controller and the interrogators.

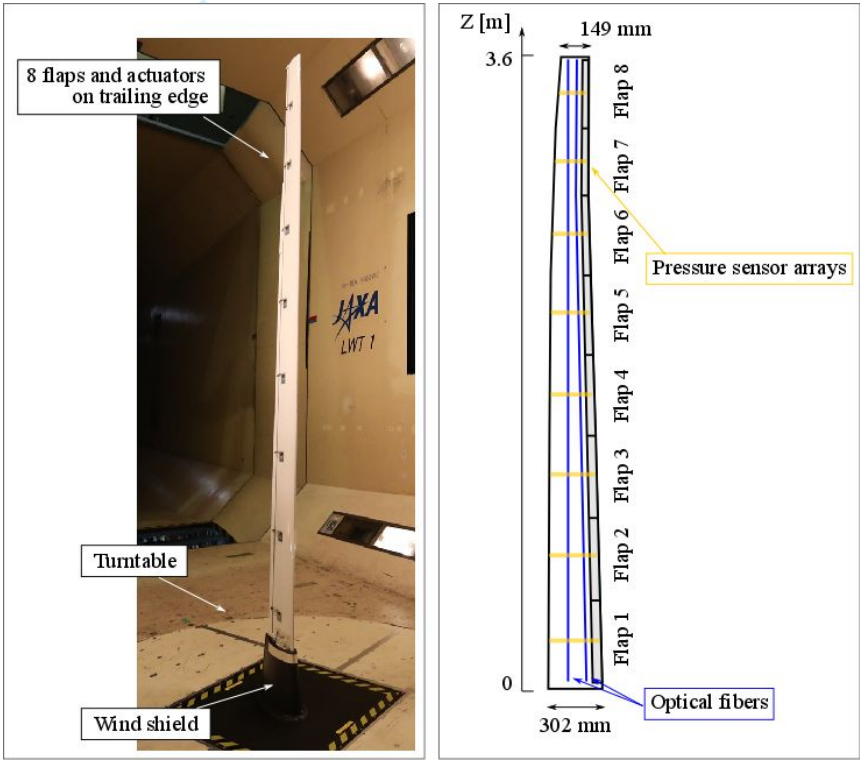


Fig. 1 Wing model. Left: Photograph in wind tunnel taken from upstream and lower side of wing. Right: Schematic of flaps and sensors viewed from upper side of wing.

Table 1 Wing geometry

| Segment No. | Position Z of flap center, m | Span-wise flap length, m | Chord length, mm | Flap width, mm |
|-------------|------------------------------|--------------------------|------------------|----------------|
| 1 | 0.277 | 0.472 | 297 | 54 |
| 2 | 0.749 | 0.472 | 283 | 51 |
| 3 | 1.221 | 0.472 | 271 | 48 |
| 4 | 1.686 | 0.458 | 258 | 45 |
| 5 | 2.144 | 0.458 | 243 | 43 |
| 6 | 2.602 | 0.458 | 226 | 40 |

| | | | | |
|---|-------|-------|-----|----|
| 7 | 3.025 | 0.388 | 208 | 39 |
| 8 | 3.413 | 0.388 | 186 | 37 |

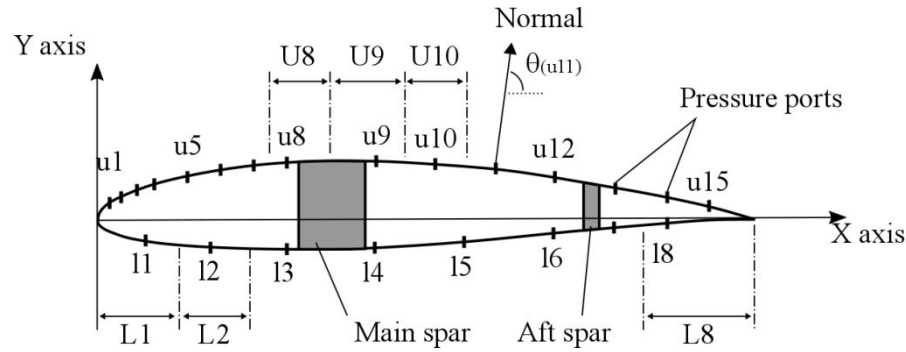


Fig. 2 Cross-section of wing model with locations of pressure ports and spars.

Table 2 Pressure port geometry. C represents chord length.

| Port | Position X/C | Position Y/C | Normal direction θ , deg |
|-----------------|-------------------|-------------------|------------------------------------|
| (leading edge) | 0 | 0 | 180 |
| u1 | 0.02 | 0.024 | 125 |
| u2 | 0.03 | 0.037 | 117 |
| u3 | 0.06 | 0.047 | 110 |
| u4 | 0.08 | 0.057 | 107 |
| u5 | 0.13 | 0.067 | 102 |
| u6 | 0.19 | 0.077 | 98 |
| u7 | 0.24 | 0.084 | 96 |
| u8 | 0.29 | 0.088 | 94 |
| u9 | 0.42 | 0.088 | 90 |
| u10 | 0.52 | 0.084 | 87 |
| u11 | 0.61 | 0.077 | 84 |
| u12 | 0.70 | 0.064 | 82 |
| u13 | 0.79 | 0.047 | 80 |
| u14 | 0.87 | 0.034 | 79 |
| u15 | 0.93 | 0.020 | 77 |
| b1 | 0.07 | -0.030 | 260 |
| b2 | 0.17 | -0.040 | 267 |
| b3 | 0.29 | -0.044 | 270 |
| b4 | 0.42 | -0.040 | 273 |
| b5 | 0.56 | -0.034 | 275 |
| b6 | 0.70 | -0.020 | 276 |
| b7 | 0.79 | -0.013 | 276 |
| b8 | 0.87 | -0.0067 | 274 |
| (trailing edge) | 1 | 0 | 0 |

| | | | |
|-------------|-------------|----------------|---|
| (main spar) | 0.30 - 0.40 | -0.043 - 0.091 | - |
| (aft spar) | 0.74 - 0.76 | -0.017 - 0.057 | - |

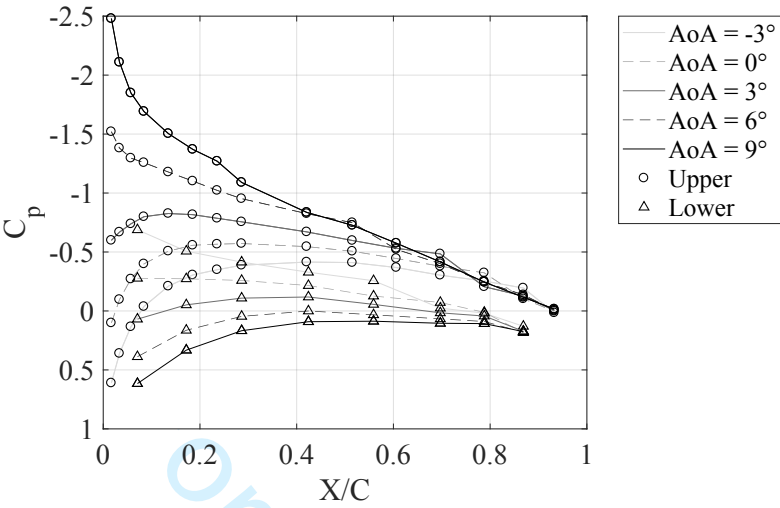


Fig. 3 Pressure coefficient distribution.

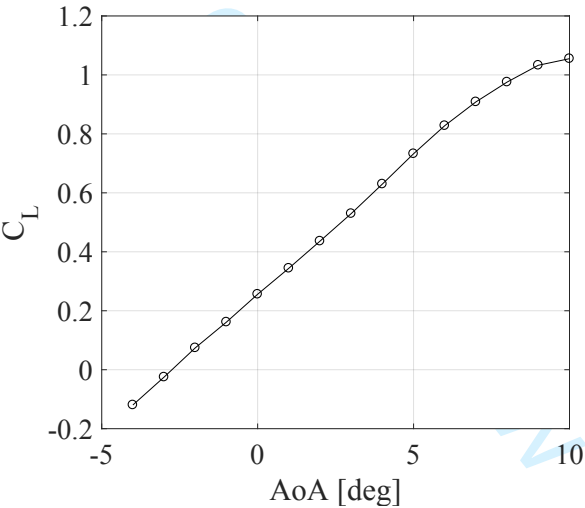


Fig. 4 Lift coefficient versus AoA.

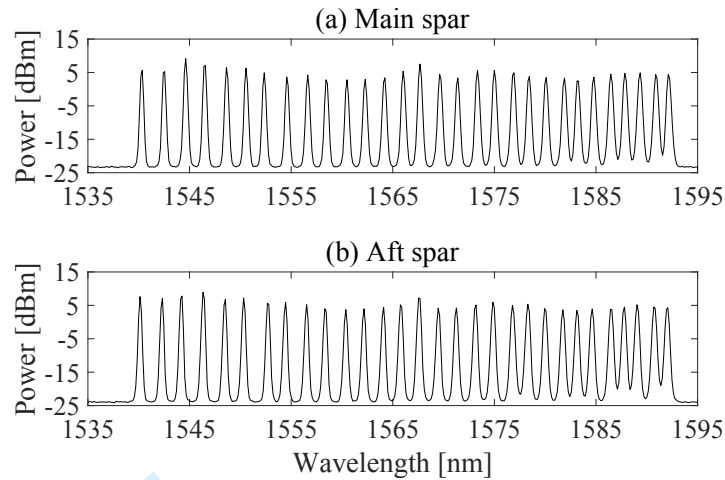


Fig. 5 Reflected spectra from optical fiber sensors bonded along main (a) and aft (b) spars.

B. Wind Tunnel Test

We applied aerodynamic loads to the wing model by wind tunnel tests. Figure 1 (left) is a photograph of the wing in the closed-circuit wind tunnel. The wind tunnel test section was 6.5 m high and 5.5 m wide. We changed the AoA by rotating the turntable. A constant wind speed of 14 m/s and a dynamic pressure of 118.7 Pa were used in the following experiments. Reynolds number was 2×10^5 .

A total of 586 test cases were conducted. The details of the test cases are presented in Table 3. Combinations of flap angles were used for each AoA cases for the individual test types. The flap angles were maintained for approximately 10 s for each test case, and visual checks were conducted to ensure that there was no vibration on the wing model. In this manner the measurements were performed without any dynamic effects. In the “aligned” test cases, all eight flap angles were set to 0° , and tests were conducted for 15 AoAs ranging from -4.0 – 10.0° with 1° intervals. In the “random” test cases, we aimed to apply 10 pseudo-random combinations of flap angles for 29 AoA cases ranging from -4.0 – 10.0° with 0.5° intervals. In order to avoid large changes in flap angles in a single test step that could result in large amplitudes of vibrations during testing, constant intervals of the flap angle variations between each test case were set, as presented in Table 4. We aimed to minimize the flap angle variation rate, specifically at the wing tip (i.e., Flap 8) where the greatest moments were found. Figure 6 shows examples of the Flaps 1, 4, and 7 angles for a number of the sequential “random” test cases. The flap angles “rebounded” within the range -15 – 15° . The bias remained in individual AoA cases (29 cases), although it was felt that the angle combinations were fully investigated across the 290 “random” case measurements. The primary aim of the “random” test cases was to obtain sufficient amounts of training data for the subsequent machine learning. In the “single” cases, a single flap was moved for eight

AoAs ranging from -4.0° – 10.0° with 2.0° intervals. In the individual AoA cases, we moved a single flap through -15.0° , -5.0° , 5.0° , and 15.0° while the other flaps remained at 0° degrees. This sequence was repeated for all eight flaps. It was anticipated that the “single” test cases would highlight the effect of individual flaps on the aerodynamic load distributions. In “controlled” cases, a flap angle combination was applied as presented in Table 5. The flap angle combination was designed to reduce the moment while maintaining the lift force. The wing root tended to increase the lift force while the wing tip tended to decrease the moment. Measurements were conducted for 14 AoA cases ranging from -4.0° – 10.0° with 1.0° intervals. We did not conduct measurements at $\text{AoA} = 4.0^{\circ}$ as undamped wing vibration occurred. It was surmised that the vortex around the wing caused the resonance. The “controlled” cases were aimed at identifying the optimum load distribution control, therefore, it was regarded as target data to be identified.

The efficiency of the acquisition of the training data is important from the practical point of view. The “aligned,” “random” and “single” test cases were designed to enable us acquire data with simple maneuvers. It was only needed to preset the angle increments for single or all flaps between each test cases, and the data was obtained automatically at individual test cases. There was no overlapping of the cases.

For each test case the Bragg wavelengths, which correspond to strains, and pressures from which lift load distributions were calculated, were measured. We also recorded the AoA and the eight flap angles.

Table 3 Test cases

| Type | AoA, deg | Number of measurements at each AoA | Total number of measurements |
|------------|---|---------------------------------------|---------------------------------|
| Aligned | -4.0, -3.0, -2.0, ..., 10.0 (15 cases) | 1 | 15 |
| Random | -4.0, -3.5, -3.0, ..., 10.0 (29 cases) | 10 | 290 |
| Single | -4.0, -2.0, -0.0, ..., 10.0 (8 cases) | 32 | 256 |
| Controlled | -4.0, -3.0, -2.0, ..., 10.0 (14 cases*) | 1 | 14 |

*We did not conduct measurements at $\text{AoA} = 4.0^{\circ}$.

Table 4 Flap angle variation rate for “random” test cases

| Flap No. | Flap angle variation rate, deg/test case |
|----------|---|
| 1 | 9.8 |
| 2 | 7.2 |
| 3 | 5.7 |
| 4 | 4.8 |
| 5 | 3.6 |
| 6 | 2.6 |
| 7 | 1.9 |
| 8 | 1.2 |

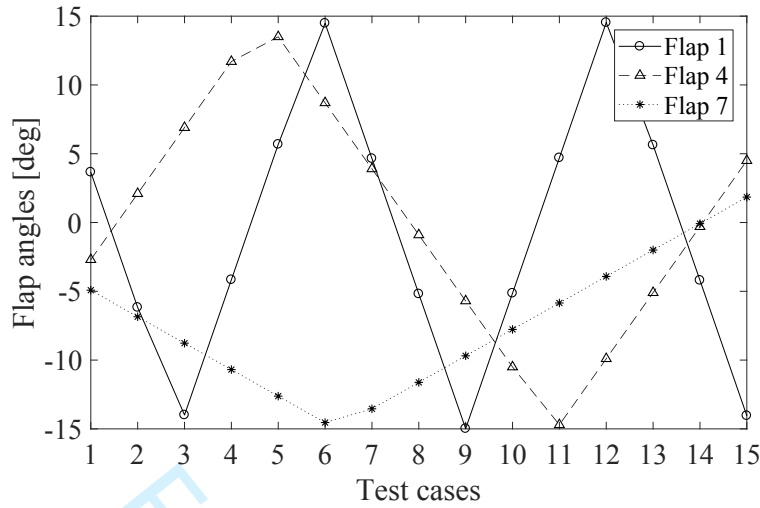


Fig. 6 Examples of flap angles for “random” test cases.

Table 5 Flap angle combination for “controlled” test cases.

| Flap No. | Flap angle [deg] |
|----------|------------------|
| 1 | 15.0 |
| 2 | 15.0 |
| 3 | 13.0 |
| 4 | 0.8 |
| 5 | -12.1 |
| 6 | -15.0 |
| 7 | -15.0 |
| 8 | -15.0 |

C. Load Identification Method

In a mechanical relationship, strains are induced by loads, which is expressed as

$$\boldsymbol{\varepsilon} = \mathbf{S}\mathbf{L}, \quad (1)$$

where $\boldsymbol{\varepsilon}$ is strain vector, \mathbf{L} is load vector and \mathbf{S} is a transfer matrix. This is a direct problem where loads are input and strains are output. When applied loads are to be identified from measured strains, it raises inverse problem as

$$\mathbf{L} = \mathbf{S}^+ \boldsymbol{\varepsilon}, \quad (2)$$

where \mathbf{S}^+ is a generalized inverse matrix of \mathbf{S} . In order to avoid the inverse analysis that is unstable to solve, the neural network approach was employed in this study. The neural network is used to replace \mathbf{S}^+ as

$$\mathbf{L} = NN(\boldsymbol{\varepsilon}), \quad (3)$$

where $NN(x)$ expresses the output of a neural network when x was the input. In this approach, the strain-to-load transfer is not represented by the inverse matrix but by the neural network. The neural network is optimized in a direct problem where strains are input and loads are output. Therefore, stable solutions are expected.

We created a neural network to calculate the lift load distribution. The architecture of the neural network, which was a feed-forward neural network with 1 hidden layer, is depicted in Fig. 7. The input layer had 68 neurons, the hidden layer 12 neurons, and the output layer eight neurons, and they were fully-connected. The number of nodes and layers were determined experimentally. For the input layer, we used data from 60 FBGs bonded along the main and aft spars, as well as data of the eight flap angles. It was evident that the strain had a mechanical cause-and-effect (or rather effect-and-cause) relationship and, therefore, the FBG signals should be used for load identification. Theoretically, the input of the strain information should be sufficient for the load identification as seen in Eq. (3), however, we anticipated that the strain would be less sensitive to the local lift load for example at the wing root due to the high stiffness. In order to enhance the sensitivity between the input and output of the neural network, the flap angle information was added as an input in this study. Therefore, the load identification process is redefined as

$$\mathbf{L} = NN_{load}(\boldsymbol{\epsilon}, \boldsymbol{\delta}), \quad (4)$$

where $\boldsymbol{\delta}$ is the eight flap angles. The FBG signal, which is the Bragg wavelength shift from a reference condition, is typically converted to strain values by using a wavelength-strain coefficient, however, the physical unit was irrelevant in this instance of machine learning. Therefore, we used the raw Bragg wavelength shifts in wavelength units. The reference Bragg wavelengths were the resting state of the wing without wind. We used sigmoid transfer functions (hyperbolic tangent) in the hidden layer and a linear function in the output layer. The eight outputs corresponded to the lift load on the eight span-wise wing segments. The Levenberg–Marquardt backpropagation algorithm [25] was used as an optimizer and the Nguyen–Widrow initialization method [26] was used to initialize weights and biases. The learning parameters used are identical to those used in a previous study [25].

Test cases of “aligned,” “random,” and “single” were used as training data to train the neural network. The “controlled” cases were excluded so that they could be treated as new conditions for the neural network after training. For the training data, we used “aligned,” “single,” and 80% (232 cases) of the “random” test cases for optimization iterations. The balance of the “random” test cases were used for validation purposes in order to avoid overfitting. The loss of the validation data was monitored during the optimization iterations. When the loss of the validation data increased across five sequential iterations, the optimization process was stopped and the weights and biases at the minimum loss were selected.

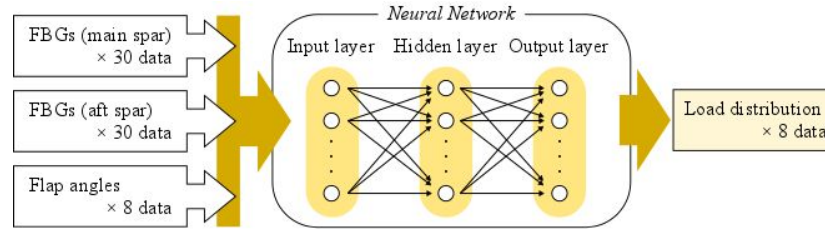


Fig. 7 Architecture of neural network for load identification.

III. Results: Load Identification

Measurements were conducted for the planned test cases. As an example of the wing deformation, the measured strain distributions for $\text{AoA} = -4^\circ$ and 10° in the “controlled” cases are shown in Fig. 8. In order to better understand the mechanical implication of the data, we converted the measured Bragg wavelength shifts to strain values by using the Bragg wavelength-strain coefficient of $827 \mu\epsilon/\text{nm}$. In general, the amplitudes of strain variations were greater for the main spar than the aft spar due to the thickness difference under wing deflection. The strain amplitude was smaller at the wing tip, and this was in good agreement with typical strain distributions of a cantilever beam. However, the strain amplitude decreased at the wing root because of the greater cross-sectional area as well as the 400-mm stainless-steel shaft inserted at the wing root that increased the stiffness. The maximum strain amplitude was observed at approximately 400 mm. In the case of $\text{AoA} = -4^\circ$, it exhibited tensile strains, which indicated that the wing model deflected downward. In the case of $\text{AoA} = 10^\circ$, it exhibited compressive strains as the wing model deflected upward.

The neural network was trained using the measured data. Thereafter, we used the trained neural network to identify load distributions. Figure 9 shows examples of the load identification results for the test cases used to train the neural network. We plotted an “aligned” test case where $\text{AoA} = 0^\circ$ and “single” test cases with $\text{AoA} = -4^\circ$ and Flap 2 at 15° , and $\text{AoA} = 4^\circ$ and Flap 7 at -15° . In the “aligned” test case, the load distribution was relatively uniform, however, in the “single” test cases, load variations were observed at the repositioned flaps. Positive flap angle of Flap 2 at $\text{AoA} = -4^\circ$ produced a lift increase and negative flap angle of Flap 7 at $\text{AoA} = 4^\circ$ a decrease in lift. The lift variations were observed locally at the wing segments with the repositioned flaps. The three plots also indicated that greater AoA values produced greater lift loads. The solid lines represent the estimated loads and the dashed lines the applied loads that were calculated from the pressure values, and there is good agreement between them. This indicated that the neural network training was satisfactorily completed and the neural network could be applied to the load identification problem. In order to examine the neural network performance for new conditions, we input the FBG and flap angle data of the “controlled” test cases, which were not used for the training. Figure 10 shows the load identification results

1
2
3
4
5
6
7
8
9
10
11
12
13
14
15
16
17
18
19
20
21
22
23
24
25
26
27
28
29
30
31
32
33
34
35
36
37
38
39
40
41
42
43
44
45
46
47
48
49
50
51
52
53
54
55
56
57
58
59
60

for $AoA = -4^\circ$ and 10° . It could be seen that for the “controlled” flap angles, the wing root was subjected to greater lift loads and the wing tip to smaller or negative lift loads. The total lift loads increased with increasing AoA . The solid lines represent the estimated loads and the dashed lines the applied loads. The results were in good agreement, which indicated that the neural network successfully learned to generalize unexperienced conditions. The errors appeared greater for the data not used for training, and thus for a quantitative comparison, we plotted the estimated loads with regard to the applied loads in Fig. 11. The load values correspond to the lift loads on the individual wing segments. The black circles represent the results for the training data that includes the “aligned,” “random,” and “single” test cases. The red squares represent the results for other data, the “controlled” test cases. The error ranges were from -0.89 – 0.84 N and from -1.5 – 1.4 N for the training and other data, respectively. The standard deviations of the errors were 0.14 N and 0.57 N for the training and other data, respectively. The slight difference of the accuracy between the training and other data reflected that the neural network output better results for the data used for training. This also indicated that the load identification performance would be improved by adding load cases of interest to training data set.

In the experiment, the out-of-plane forces of the wing model were identified as the lift loads. On the other hand, the in-plane forces were applied to the wing model, which were out of focus in this study. The major reason was that the applied in-plane forces were unavailable. The in-plane force consisted of the in-plane component (X-component in Fig. 2) of the pressure values and the friction drag, which were difficult to directly and accurately measure simply by the equipped pressure ports. If the applied in-plane forces were measured and the training data were prepared, the in-plane forces would potentially be identified through the same identification process. By identifying both the out-of-plane and in-plan forces of the wing, the lift and drag forces for aircraft would be estimated.

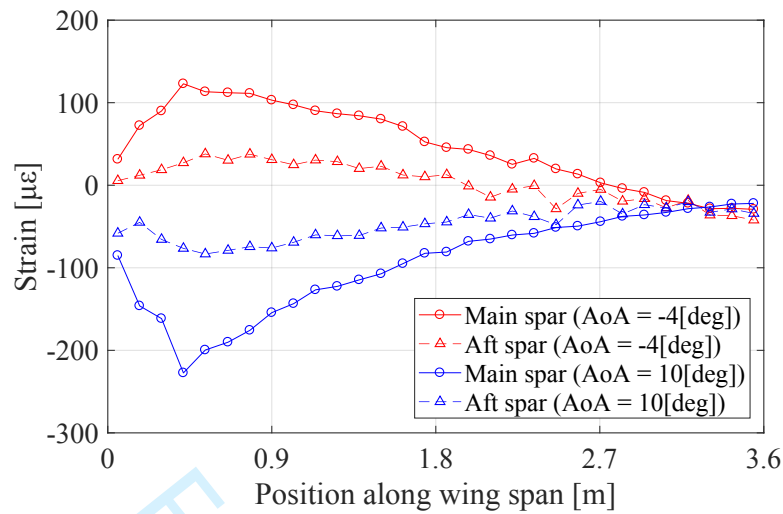


Fig. 8 Measured strain distributions at $AoA = -4^\circ$ and 10° in “controlled” test cases.

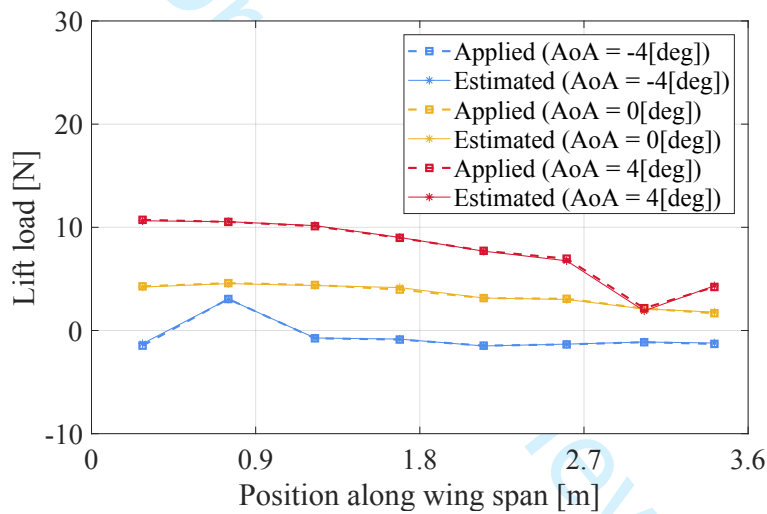


Fig. 9 Load identification results in “aligned” test case ($AoA = 0^\circ$) and “single” test case ($AoA = -4^\circ$ and 4°). Flap 2 angle 15° when $AoA = -4^\circ$, and Flap 7 angle -15° when $AoA = 4^\circ$.

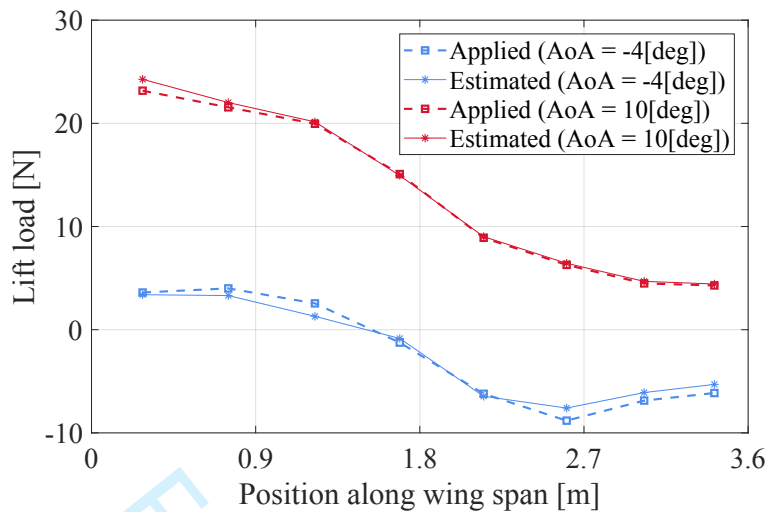


Fig. 10 Load identification results in “controlled” test cases with AoA = -4° and 10°.

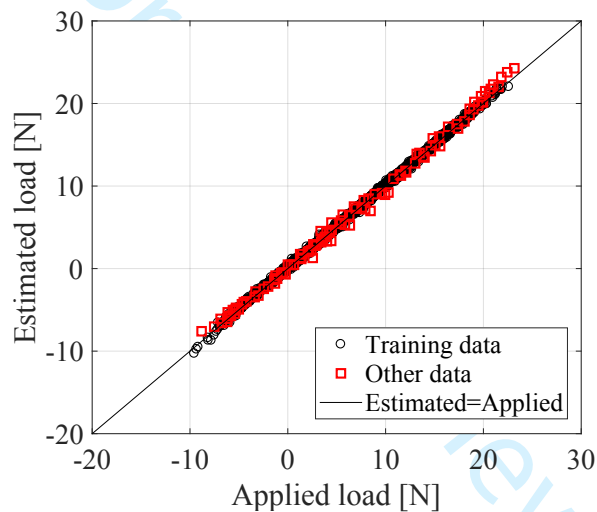


Fig. 11 Comparison between applied and estimated loads.

IV. Discussion: AoA Identification

Loads and strains were in a mechanical cause-and-effect relationship, therefore, the neural network was an applicable modeling method. At the same time, the lift load distribution, \mathbf{L} , are expressed in an aerodynamic cause-and-effect relationship as

$$\mathbf{L} = q\mathbf{C_L}(\boldsymbol{\delta},\alpha)\mathbf{A}, \quad (5)$$

where q is the dynamic pressure, α is the AoA, $\mathbf{C_L}$ is the lift coefficients and \mathbf{A} is the areas of the wing segments. In the experiment, we could assume that the dynamic pressure q and the wing areas \mathbf{A} were constant, and the $\mathbf{C_L}$ was a function of the flap angles $\boldsymbol{\delta}$ and the AoA α . The variables in the aerodynamic relationship were the lift loads \mathbf{L} , the

flap angles δ and the AoA α . Therefore, it was anticipated that the neural network was applicable to predict AoA from the lift loads and the flap angles as expressed as

$$\alpha = NN(\mathbf{L}, \delta), \quad (6)$$

where α is the AoA. We would be able to identify α not by solving Eq. (5) in an inverse manner but by using a neural network. We designed a neural-network-based identification process for the AoA as shown in Fig. 12. In this design, we identify load distributions by using the 60 FBGs (strain) and flap angle data through the neural network for the load identification as discussed above, and thereafter we identify the AoA by using the identified load distribution and the flap angles through another neural network for the AoA identification. This process requires only the FBG and flap angle data to be observed, which is a feasible assumption.

The neural network for the AoA identification had 1 hidden layer with 10 neurons, which was determined experimentally. We set other properties and training parameters in the same way as the load identification. In order to train the neural network for the AoA identification, we prepared a dataset of flap angles and estimated loads, which were the output from the neural network for the load identification, for the training test cases (“aligned,” “random,” and “single”). The other cases (“controlled”) were used to check the performance from the new conditions. Figure 13 shows the results of the neural network AoA predictions. The error ranges were from -0.78 – 0.46° and from -1.03 – 0.16° for the training and other data, respectively. The standard deviations of the errors were 0.15° and 0.38° for the training and other data, respectively. These results indicated a successful AoA identification.

Because of limitations of the experimental setup, we observed the AoA at the turntable. If we could measure the profile of the AoA along the wing span, the neural network approach might be capable of identifying local AoAs, which would contribute to the development of effective wing twist techniques.

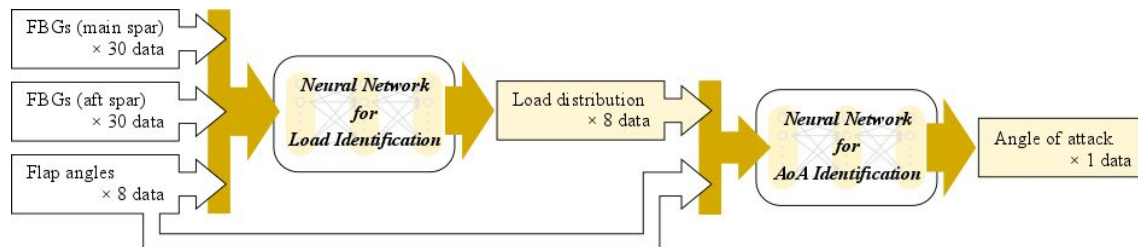


Fig. 12 Design of NN-based identification process for load and AoA.

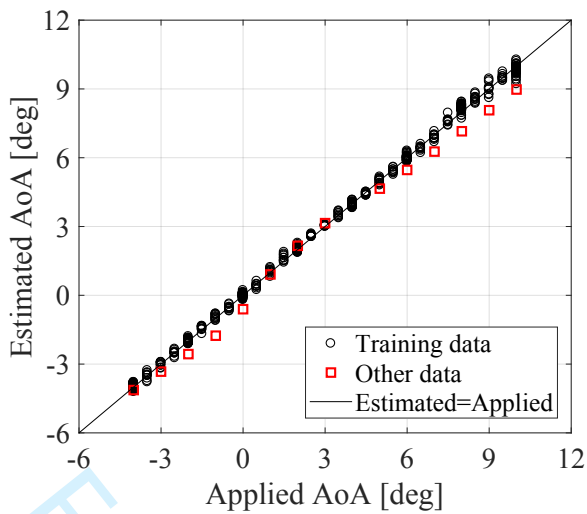


Fig. 13 Comparison between applied and estimated AoA.

V. Discussion: Wind Speed Variation

For the results above, the constant wind speed 14 m/s and a dynamic pressure of 118.7 Pa were assumed. As a discussion, we investigated the identification performances when variations of wind speeds existed. We conducted additional “random” test cases for the wind speeds 13, 12, 11 and 10 m/s where dynamic pressures were 103.0, 87.28, 73.50 and 60.80 Pa, respectively. In each wind speed, we applied 10 pseudo-random combinations of flap angles for 29 AoA cases ranging from -4.0 – 10.0° with 0.5° intervals as was the case of 14 m/s, which resulted in 1160 additional test cases. We used the neural networks previously described, which were trained using the data at the constant wind speed 14 m/s. Figure 14 and 15 show representative load and AoA identification results under the wind speed variations, respectively. The AoA identification performance evidently degraded in accordance with the wind speed variation, as the estimated AoAs at lower wind speeds tended to be smaller specifically at a large AoA range. On the other hand, the load identification performance did not exhibit significant variations for different wind speeds. These results highlighted the difference of what the neural networks represented in the identification processes. The mechanical strain-load relationship was independent from the wind speed as expressed in Eq. (2), therefore the neural network trained at the wind speed 14 m/s was valid for different wind speeds in theory. On the other hand, the aerodynamic relationship among the AoA, loads and flap angles depended on the wind speed, or in other words the dynamic pressure as expressed in Eq. (5), therefore the output of the neural network for the AoA identification became erroneous when the wind speed varied. The neural-network-based identification in Eq. (6) was not valid when the constant dynamic pressure was not assumed.

When the dynamic pressure q was also assumed as a variable in Eq. (5), the AoA identification could be expressed as

$$\alpha = NN(\mathbf{L}, \delta, q). \quad (7)$$

The valid AoA identification was expected by including the dynamic pressure q in the input. We prepared a dataset of flap angles, estimated lift loads and dynamic pressure for the training test cases that included “aligned,” “random,” and “single” cases for the wind speed 14 m/s and “random” cases for the wind speeds 13, 12, 11 and 10 m/s. Using the data set, we trained the neural network for the AoA identification again. Figure 16 shows the representative results of the AoA predictions with dynamic pressure input. The evident improvement of the AoA identification performance was observed. For reference, we also conducted training of the neural network using the same dataset but not including the dynamic pressure input. Figure 17 shows the results of the AoA predictions. The identification accuracy was improved from Fig. 15, however, it was not as high as the one with the dynamic pressure input. These results indicated that the neural network for the AoA identification should have the input of wind speeds (dynamic pressures). It was evident that the larger amount and ranges of training data contribute to better performance of neural networks. In addition, it was essential to distinguish which parameters were to be observed and used for training based on physical backgrounds of identification processes.

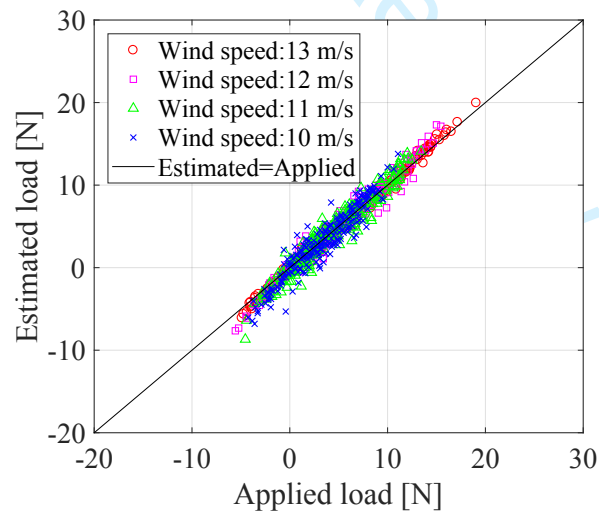


Fig. 14 Comparison between applied and estimated loads for different wind speeds.

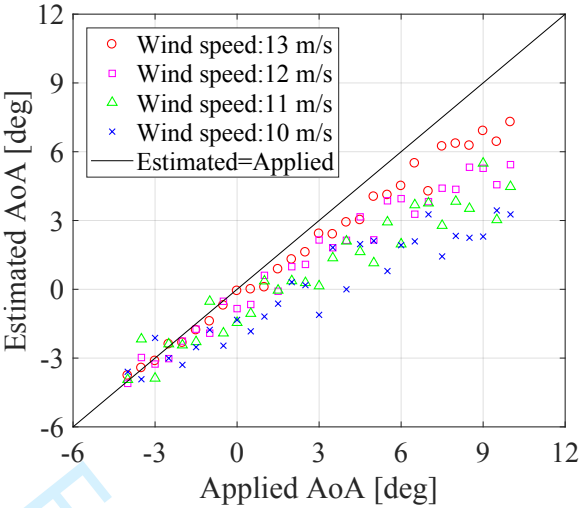


Fig. 15 Comparison between applied and estimated AoA for different wind speed.

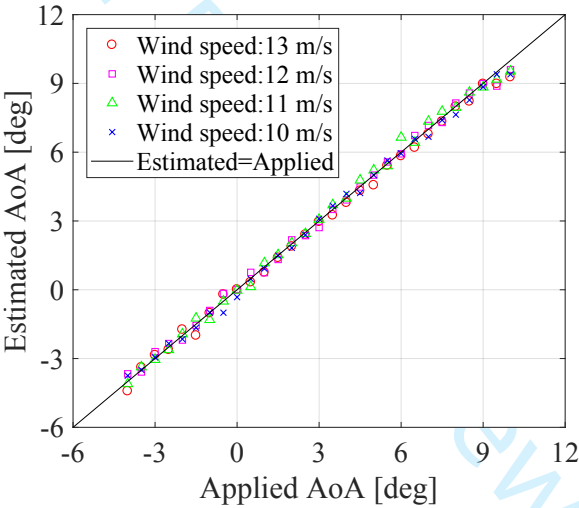


Fig. 16 Comparison between applied and estimated AoA by neural network trained by dataset including different wind speeds with dynamic pressure input.

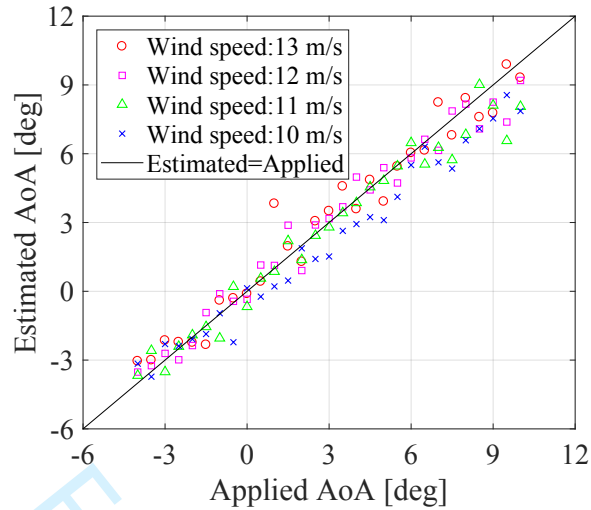


Fig. 17 Comparison between applied and estimated AoA by neural network trained by dataset including different wind speeds without dynamic pressure input

VI. Conclusions

We developed a 3.6 m semi-spanned wing model with eight trailing edge flaps. Two optical fibers with 30 FBGs were bonded on the upper side of the wing model along the main and aft spars. Aerodynamic loads were applied to the wing model by wind tunnel tests, and load identification was performed by using the neural network approach. The FBG data and the eight flap angles were input to the neural network, and the estimated load distributions on the eight wing segments were output. The load distributions were successfully identified, even for data that were not used for training of the neural network. The error range was from -1.5–1.4 N with a standard deviation of 0.57 N.

We also investigated the neural-network-based identification process for AoA. In this process, load distributions were first identified, and thereafter the AoA was determined by using the load distributions and the flap angles through another neural network. This process required only the FBG and flap angle data to be observed. The neural network successfully identified the AoA with error ranges from -1.03–0.46° with a standard deviation of 0.38°.

We discussed the identification performances when the variations of wind speeds existed. Compared with the load identification, the performance of the AoA identification degraded in accordance with the wind speed variation. It was because the mechanical strain-load relationship was independent from the wind speed whereas the aerodynamic relationship among the AoA, loads and flap angles depended on the wind speed. **By including the dynamic pressure information in the neural network input, the performance of the AoA identification was improved for the variations of wind speeds.** It was highlighted that we need to distinguish which parameters are to be observed and used for training based on physical backgrounds of identification processes.

Funding Sources

This work was supported by JSPS KAKENHI Grant Number JP17K14878.

References

[1] Nguyen, N., Ting, E., Chaparro, D., Drew, M., and Swei, S., “Multi-objective flight control for drag minimization and load alleviation of high-aspect ratio flexible wing aircraft,” *Proceedings of 58th AIAA/ASCE/AHS/ASC Structures, Structural Dynamics, and Materials Conference*, Denver, Colorado, 2017.
doi: 10.2514/6.2017-1589

[2] Tang, D., and Dowell, E. H., “Experimental and theoretical study on aeroelastic response of high-aspect-ratio wings,” *AIAA J.*, Vol. 39, No. 8, 2001, pp. 1430-1441.
doi: 10.2514/2.1484.

[3] Tang, D., and Dowell, E. H., “Experimental and theoretical study of gust response for high-aspect-ratio wing,” *AIAA J.*, Vol. 40, No. 3, 2002, pp. 419-429.
doi: 10.2514/2.1691.

[4] Tang, D., Grash, A., and Dowell, E. H., “Gust response for flexibly suspended high-aspect ratio wings,” *AIAA J.*, Vol. 48, No. 10, 2010, pp. 2430-2444.
doi: 10.2514/1.J050309.

[5] Mohamed, A., Massey, K., Watkins, S. and Clothier, R., “The attitude control of fixed-wing MAVs in turbulent environments,” *Progress in Aerospace Sciences*, Vol. 66, 2014, pp. 37-48.
doi: 10.1016/j.paerosci.2013.12.003

[6] Mohamed, A., Clothier, R., Watkins, S., Sabatini, R., and Abdulrahim, M., “Fixed-wing MAV attitude stability in atmospheric turbulence, part 1: Suitability of conventional sensors,” *Progress in Aerospace Sciences*, Vol. 70, 2014, pp. 69-82.
doi: 10.1016/j.paerosci.2014.06.001.

[7] Mohamed, A., Watkins, S., Clothier, R., Abdulrahim, M., Massey, K., and Sabatini, R., “Fixed-wing MAV attitude stability in atmospheric turbulence, part 2: Investigating biologically-inspired sensors,” *Progress in Aerospace Sciences*, Vol. 71, 2014, pp. 1-13.
doi: 10.1016/j.paerosci.2014.06.002.

[8] Tarantola, A., *Inverse Problem Theory and Methods for Model Parameter Estimation*, SIAM, Philadelphia, PA, 2005.

[9] Hansen, P. C., *Discrete Inverse Problems: Insight and Algorithms*, SIAM, Philadelphia, PA, 2010.

[10] Aster, R. C., Borchers, B., and Thurber C. H., *Parameter Estimation and Inverse Problems*, 2nd ed, Academic Press, Cambridge, MA, 2012.

- [11] Shkarayev, S., Krashantisa, R., and Tessler, A., "An inverse interpolation method utilizing in-flight strain measurements for determining loads and structural response of aerospace vehicles," *Proceedings of 3rd International Workshop on Structural Health Monitoring*, Stanford, California, 2001.
- [12] Coates, C. W., and Thamburaj, P., "Inverse method using finite strain measurement to determine flight load distribution functions," *Journal of Aircraft*, Vol. 45, No. 2, 2008, pp. 366-370.
doi: 10.2514/1.21905.
- [13] Nakamura, T., Igawa, H., and Kanda, A., "Inverse identification of continuously distributed loads using strain data," *Aerospace Science and Technology*, Vol. 23, No. 1, 2012, pp. 75-84.
doi: 10.1016/j.ast.2011.06.012.
- [14] Cao, X., Sugiyama, Y., and Mitsui, Y., "Application of artificial neural networks to load identification," *Computers and Structures*, Vol. 69, No. 1, 1998, pp. 63-78.
doi: 10.1016/S0045-7949(98)00085-6.
- [15] Trivailo, P. M., and Carn, C. L., "The inverse determination of aerodynamic loading from structural response data using neural networks," *Inverse Problems in Science and Engineering*, Vol. 14, No. 4, 2006, pp. 379-395.
doi: 10.1080/17415970600573692.
- [16] Wada, D., and Sugimoto, Y., "Inverse analysis of aerodynamic loads from strain information sing structural models and neural networks," *Proceedings of SPIE*, Vol. 10168, 2017, 101680W.
doi: 10.1117/12.2258583.
- [17] Carpenter, T. J., and Albertani, R., "Aerodynamic load estimation from virtual strain sensors for a pliant membrane wing," *AIAA J.*, Vol. 53, No. 8, 2015, pp. 2069-2079..
doi: 10.2514/1.J053291.
- [18] Wada, D., Igawa, H., and Kasai, T., "Vibration monitoring of a helicopter blade model using the optical fiber distributed strain sensing technique," *Applied Optics*, Vol. 55, No. 25, 2016, pp. 6953-6959.
doi: 10.1364/AO.55.006953.
- [19] Wada, D., Igawa, H., Tamayama, M., Kasai, T., Arizono, H., and Murayama, H., "Flight demonstration of aircraft wing monitoring using optical fiber distributed sensing system," *Smart Materials and Structures*, 2018. (accepted)
doi: 10.1088/1361-665X/aae411.
- [20] Pak, C., "Wing shape sensing from measured strain," *AIAA J.*, Vol. 54, No. 3, 2016, pp. 1064-1073.
doi: 10.2514/1.J053986.
- [21] Kim, J., Park, Y., Kum, Y., Shrestha, P., and Kim, C., "Aircraft health and usage monitoring system for in-flight strain measurement of a wing structure," *Smart Materials and Structures*, Vol. 24, 2015, pp.105003-1-12.

doi: 10.1088/0964-1726/24/10/105003.

[22] Kressel, I., Balter, J., Mashiach, N., Sovran, I., Shapira, O., Shemesh, N.Y., Glamm, B., Dvorjetski, A., Yehoshua, T., and Tur, M., “High speed, in-flight structural health monitoring system for medium altitude long endurance unmanned air vehicle,” *Proceedings of 7th European Workshop on Structural Health Monitoring*, Nantes, France, 2014.

[23] Lance, R., Allen, R. P. Jr., Anthony, P., Patrick, C., Harmory, P., and Pena, F., “NASA Armstrong Flight Research Center (AFRC) Fiber Optic Sensing System (FOSS) Technology,” NASA Technical Reports Server, 2014.

[24] Kersey, A. D., Davis, M. A., Patrick, H. J., LeBlanc, M., Koo, K. P., Askins, C. G., Putnam, M. A., and Friebele, E. J., “Fiber grating sensors,” *Journal of Lightwave Technology*, Vol. 15, No. 8, 1997, pp. 1442-1463.

doi: 10.1109/50.618377.

[25] Hagan, M. T., and Menhaj, M. B., “Training feedforward networks with the Marquardt algorithm,” *IEEE Transactions on Neural Networks*, Vol. 5, No. 6, 1994, pp. 989-993.

doi: 10.1109/72.329697.

[26] Nguyen, D., and Widrow, B., “Improving the learning speed of 2-layer neural networks by choosing initial values of the adaptive weights,” *Proceedings of 1990 IJCNN International Joint Conference on Neural Networks*, San Diego, CA, 1990.